Structure and transport in high pressure oxygen sputter-deposited BaSnO3−δ

Koustav Ganguly, Palak Ambwani, Peng Xu, Jong Seok Jeong, K. Andre Mkhoyan, C. Leighton, and Bharat Jalan

---

Articles you may be interested in

Dopant-site-dependent scattering by dislocations in epitaxial films of perovskite semiconductor BaSnO3
APL Mat. **2**, 056107 (2014); 10.1063/1.4874895

Electron transport and defect structure in highly conducting reactively sputtered ultrathin tin oxide films
Appl. Phys. Lett. **104**, 082108 (2014); 10.1063/1.4866869

ZnO epitaxy on (111) Si using epitaxial Lu 2 O 3 buffer layers
Appl. Phys. Lett. **92**, 072101 (2008); 10.1063/1.2841667

Low pressure oxygen annealing at high temperature for high quality sputtered YBa 2 Cu 3 O 7−δ films
Appl. Phys. Lett. **76**, 3621 (2000); 10.1063/1.126726

Oxygen pressure-tuned epitaxy and optoelectronic properties of laser-deposited ZnO films on sapphire
Appl. Phys. Lett. **75**, 3947 (1999); 10.1063/1.125503

Structure and transport in high pressure oxygen sputter-deposited BaSnO$_{3-\delta}$

Koustav Ganguly, Palak Ambwani, Peng Xu, Jong Seok Jeong,
K. Andre Mkhoyan, C. Leighton,[a] and Bharat Jalan[a]
*Department of Chemical Engineering and Materials Science, University of Minnesota,
Minneapolis, Minnesota 55455, USA*

BaSnO$_3$ has recently been identified as a high mobility wide gap semiconductor with significant potential for room temperature oxide electronics. Here, a detailed study of the high pressure oxygen sputter-deposition, microstructure, morphology, and stoichiometry of epitaxial BaSnO$_3$ on SrTiO$_3$(001) and MgO(001) is reported, optimized conditions resulting in single-phase, relaxed, close to stoichiometric films. Most significantly, vacuum annealing is established as a facile route to *n*-doped BaSnO$_{3-\delta}$, leading to electron densities above 10^{19} cm^{-3}, 5 mΩ cm resistivities, and room temperature mobility of 20 cm^2 V^{-1} s^{-1} in 300-Å-thick films on MgO(001). Mobility limiting factors, and the substantial scope for their improvement, are discussed. © *2015 Author(s). All article content, except where otherwise noted, is licensed under a Creative Commons Attribution 3.0 Unported License.* [http://dx.doi.org/10.1063/1.4919969]

Semiconducting oxides with predominantly *s*-orbital-derived conduction bands are attractive due to their potential for low electron effective mass and high room temperature mobility. ZnO is an illustrative example, with electron mobility up to 430 cm^2 V^{-1} s^{-1} at ambient,[1,2] increasing to 700 000 cm^2 V^{-1} s^{-1} at cryogenic temperatures,[3] enabling observation of the integer,[2] and fractional[4] quantum Hall effects. Particularly, in wide band gap cases like ZnO, such semiconductors are also of interest as transparent conductive oxides (TCOs), as part of the drive to displace indium tin oxide.[5] While much exploration of binary and ternary wide gap semiconducting oxides has been thus stimulated,[5] relatively little, *in this regard*, has been done with perovskite oxides. This is despite the remarkable chemical flexibility and functionality of perovskites, which could potentially include high mobility wide gap semiconductors. Realizing high room temperature mobility in perovskites, potentially *via s*-bands rather than *d*-derived bands, is important for several reasons. Primary among these is the need, for the advancement of oxide electronics,[6–8] to translate the extraordinary diversity in functionality that has been demonstrated in perovskite oxide heterostructures[6–8] to room temperature. A high room temperature mobility perovskite semiconductor could enable, for instance, ambient temperature high mobility oxide two-dimensional electron systems, oxide transistors, and all-perovskite spintronic devices.

In this context, the recent discovery of room temperature mobility up to 320 cm^2 V^{-1} s^{-1} in *n*-doped cubic perovskite (*Pm$\bar{3}$m*) BaSnO$_3$ (BSO) single crystals[9–11] with a band gap of 3-4 eV is significant. This is the highest reported 300 K mobility in perovskite oxides and can be compared, for instance, to <10 cm^2 V^{-1} s^{-1} in SrTiO$_3$ (STO).[12] The 300 K resistivity (∼200 μΩ cm[10,13]) and visible absorption coefficient in BSO are even competitive with existing TCOs,[5] and, critically, progress has been made with film growth.[10,11,13–15] The latter has led to mobilities as high as 70 cm^2 V^{-1} s^{-1} at 10^{20} cm^{-3} in relatively thick epitaxial films, doped *n*-type by substitution with La (for Ba)[9,10,14] or Sb (for Sn).[13,16] The fundamental understanding of BSO has also improved, including its electronic structure in bulk,[10,17–22] heterostructure,[23,24] and film[21,25] form,

---

[a]Authors to whom correspondence should be addressed. Electronic addresses: bjalan@umn.edu and leighton@umn.edu

3, 062509-1

as well as its phonon spectrum,[17] optical properties,[10,11,17,20–22,26] scattering mechanisms,[10,13–15,27] defects,[28] and thermal stability.[9] It is understood that the conduction band is derived from Sn 5s states[10,17–25] and progress is being made in identifying mobility-limiting mechanisms in crystals[9–11] and films.[9,10,13–15,27]

There remain a number of unresolved issues, however, including the optimal choice of dopant ion and site[13] and the relative importance of phonon,[11,17] neutral impurity, ionized impurity,[9,10,27] and dislocation scattering.[13–15] The latter is significant in films because of the dislocations accommodating the lattice mismatch with the substrate, due to the dearth of perovskite substrates around the 4.116 Å BSO lattice parameter.[13–15] Additionally, while it is known that thick BSO films exhibit some instability at as low as 530 °C[9] and that bulk polycrystals are somewhat sensitive to treatment in N_2 and O_2 at 950 °C,[16] it is not yet clear how facile reduction is in BSO or whether it could provide an alternate route to n-doping. Density functional calculations[28] suggest quite high oxygen vacancy (V_O) formation energies and deep V_O donor levels, but the experimental situation is unclear.

Here, we report on a study of the growth, structure, and stoichiometry of epitaxial BSO deposited *via* high pressure oxygen sputter deposition. This is a proven method for oxides, where a high pressure (O(1 Torr)) O_2 plasma provides aggressive oxygenation, thermalized ions, and minimized resputtering. It is shown here to produce single-phase, relaxed, close to stoichiometric BSO, as characterized by high resolution wide-angle X-ray diffraction (WAXRD), grazing-incidence X-ray reflectivity (GIXR), atomic force microscopy (AFM), and scanning transmission electron microscopy (STEM). This is demonstrated on both STO(001) and MgO(001), the latter providing smaller lattice mismatch (2.3% tensile *vs.* 5.1% compressive) but with symmetry mismatch. Significantly, vacuum annealing of 300-Å-thick films on MgO(001) at 850 °C is shown to readily reduce BSO, the resulting V_O density generating a Hall electron density of 5×10^{19} cm^{-3}, 6 mΩ cm resistivity, and 20 cm^2 V^{-1} s^{-1} mobility. The transport is degenerate (in fact metallic) with positive temperature coefficient of resistivity down to 100 K. While this mobility is lower than prior thin film reports with other dopants, there remain numerous promising routes to further mobility optimization.

RF sputter deposition was done from 2" BSO targets synthesized by solid-state reaction of $BaCO_3$ and SnO_2 (99.9% purity) in air at 1200 °C, followed by cold-pressing then sintering at 1400 °C. Prior to growth, the substrates were annealed for 15 min in 1.9 Torr of O_2 at 900 °C. Films were subsequently deposited at 76 W with 550–850 °C substrate temperatures (T_{dep}) and 1.5–2.2 Torr O_2 pressures (P_{O2}), the rate (0.4–1.5 Å/min) being controlled by the source-to-substrate distance. Post-growth cooling was done in 600 Torr of O_2. WAXRD (including rocking curves (RCs) and reciprocal space maps (RSMs)) and GIXR were performed with Cu K_α radiation in a Panalytical X'Pert system. GenX[29] was used for GIXR refinement. Contact mode AFM was carried out in a Bruker Nanoscope V Multimode 8, while cross-sectional high-angle annular dark-field (HAADF) STEM was performed on an aberration-corrected monochromated FEI Titan G2 60–300 at 300 kV. The semi-convergent angle of the incident beam was 24.5 mrad, HAADF images were obtained with a detector angle of 50–200 mrad, and samples were tilted to a [100] zone axis. Vacuum annealing was done at 600-900 °C for 4 h at pressures $<10^{-7}$ Torr. Subsequent electronic transport measurements (AC and DC, 2-300 K, 0-9 T) utilized In contacts in a van der Pauw geometry.

To illustrate the basic structural features of high pressure oxygen sputter-deposited BSO, WAXRD for 230-Å-thick films on STO(001) and MgO(001) is shown in Figs. 1(a) and 1(b). These films were deposited at 750 °C,[10,14,26] in 1.5 Torr of O_2 (typical for this method). Figs. 1(a) and 1(b) reveal only the BSO, STO, and MgO 00l reflections, establishing phase purity (within detection limits), and out-of-plane epitaxy. Grazing incidence diffraction (supplementary material[30] Fig. S1) confirms in-plane cube-on-cube epitaxy. As can be seen from the 002 close-ups in the insets to Figs. 1(a) and 1(b), finite-size fringes are observed on STO(001), but not on MgO(001), indicating that films on STO are smoother on short lateral length scales. As shown in Fig. 1(c), however, BSO films on both substrates are smooth on the long lateral scales probed in GIXR; the fits refine the film RMS (root-mean-square) surface roughnesses to 6.8 Å on STO and 5.4 Å on MgO, i.e., the 1-2 unit cell level.

Data of the type shown in Figs. 1(a) and 1(b) also provide the out-of-plane lattice parameter (a_{op}), a probe of stoichiometry and strain state. In Fig. 2, this is plotted *vs.* P_{O2}, deposition rate, and
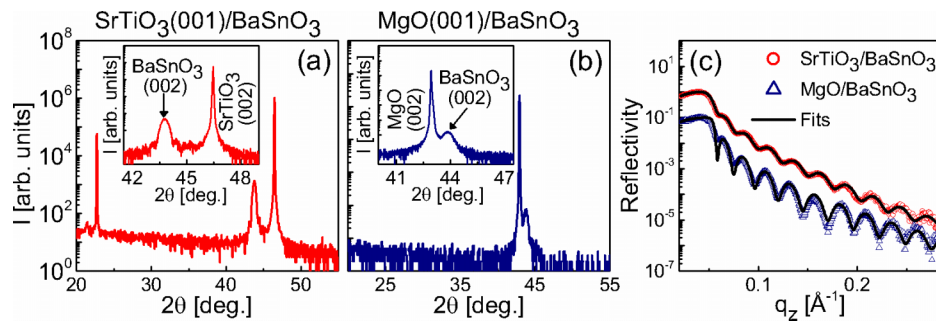
FIG. 1. Structural characterization of 230-Å-thick BSO films grown on STO(001) (red) and MgO(001) (blue) at 750 °C and 1.5 Torr O_2 pressure. High resolution WAXRD on (a) STO(001)/BSO and (b) MgO(001)/BSO. Insets: close-ups around the 002 film/substrate peaks. (c) GIXR (reflectivity *vs.* scattering wavevector, q_z) for the same films (points) along with GenX fits (solid lines). The curves are displaced for clarity. The refined film densities and surface roughnesses are 6.9 g cm^{-3} and 6.8 Å on STO(001) and 7.4 g cm^{-3} and 5.4 Å on MgO(001), respectively. The bulk density of BSO is 7.2 g cm^{-3}.

T_{dep} for films of approximate thickness (t) 100-150 Å on both STO(001) and MgO(001). The values of the deposition parameters that are held constant are shown at the top of each panel. There are two notable features in these data. First, a_{op} is similar on STO and MgO, in almost all cases lying between 4.125 and 4.140 Å, despite the very different lattice mismatch. These values are close to, but greater than (by 0.01–0.02 Å), the bulk lattice parameter[9,11,16] (horizontal line). Second, there is a remarkable insensitivity to growth conditions over the probed parameter space. One simple interpretation is that, in this thickness range, the films on both substrates are already strain relaxed. The slightly elevated a_{op} could then indicate some level of cation non-stoichiometry (potentially from the ceramic target) or non-negligible defect density.

Thickness-dependent strain relaxation was thus probed (Fig. 3) using BSO deposited on STO(001) at 750 °C in 1.5 Torr of O_2. In this figure, panels (a) through (c) plot a_{op}, the Scherrer length Λ (i.e., the 002 WAXRD peak width converted to a length *via* the Scherrer equation) and the 002 film RC full-width at half-maximum (FWHM). Two values of the latter are plotted, as t-dependent 002 RCs (supplementary material[30] Fig. S2) reveal a sharp peak superimposed on a broader one. To facilitate the discussion of strain state, Fig. 3(a) also shows the bulk lattice parameter, as well as the critical thickness for strain relaxation (t_{crit}) from the Matthews-Blakeslee formula, using the literature parameters.[18] Although this t_{crit} is rather approximate for perovskites, it is nevertheless instructive to note that it is as low as 25 Å, due to the large mismatch. The data in Fig. 3(a) are indeed consistent with low t_{crit}; a_{op} decreases with increasing t from the lowest thicknesses probed, levelling off at $a_{op} \approx 4.13$ Å for $t \geq 150$ Å. It is noted (i) that this a_{op} is consistent with Fig. 2 and (ii) that no reliable lattice parameters could be extracted below 80 Å. That films on STO above $t \approx 150$ Å are indeed relaxed is confirmed by asymmetric (013) RSMs (Fig. 3(d),
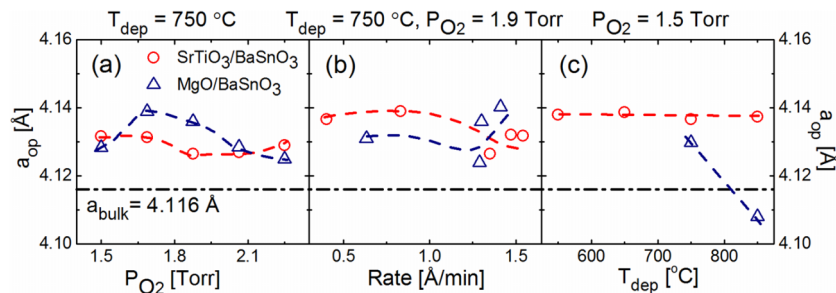

FIG. 2. Out-of-plane lattice parameter, a_{op}, *vs.* (a) O_2 growth pressure (P_{O2}), (b) deposition rate, and (c) deposition temperature (T_{dep}), for ~100–150-Å-thick BSO films on STO(001) (red) and MgO(001) (blue). In each panel, the growth parameter(s) held fixed is labeled at the top. Error bars are comparable to the symbol size. The bulk BSO lattice parameter is shown by the dashed-dotted line. Dashed lines through the data are guides to the eye.
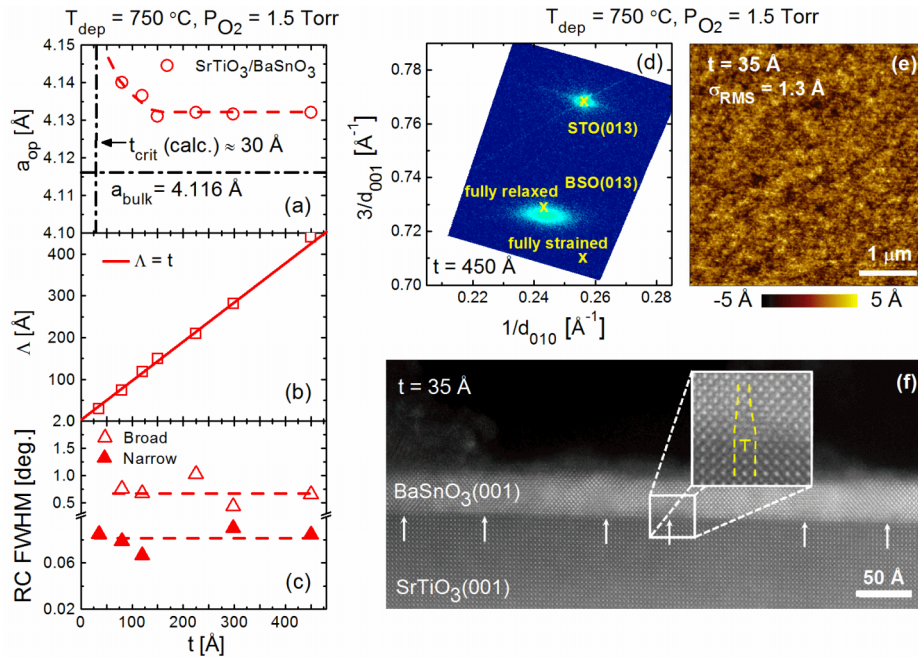
FIG. 3. Thickness dependence of (a) the out-of-plane lattice parameter, a_{op} (error bars are comparable to the symbol size) (b) the Scherrer length, Λ (i.e., the 002 WAXRD peak width converted to a length scale *via* the Scherrer equation), and (c) the two rocking curve FWHMs. All data are for STO(001)/BSO films deposited at 750 °C and 1.5 Torr. Dashed lines are guides to the eye. The dashed-dotted lines in (a) mark the bulk lattice parameter and calculated critical thickness, while the solid line in (b) is $\Lambda = t$. (d) Asymmetric reciprocal space map around the 013 reflection for a 450 Å film. Crosses mark the expected positions of fully strained and fully relaxed BSO. (e) Contact mode AFM image of a 35-Å-thick film. (f) Cross-sectional HAADF STEM image of a 35 Å film. Arrows mark misfit dislocations. Inset: magnified view of a misfit edge dislocation with Burger's vector $a[100]$.

(t) = 450 Å), where the expected reflections from relaxed and fully strained (i.e., pseudomorphic) films are marked. The BSO peak is close to the fully relaxed position, but with minor lattice expansion. This is ascribed to minor cation non-stochiometry or defect formation, as returned to below. The t dependence of a_{op} was also studied on MgO (supplementary material[30] Fig. S3), full strain relaxation occurring by ~150 Å.

The t-dependence of the Scherrer length, Λ (Fig. 3(b)) further supports very low t_{crit} on STO(001). Specifically, Λ is found to almost exactly coincide with the thickness (the solid line in Fig. 3(b) is $\Lambda = t$), meaning that the WAXRD widths are finite size dominated, with negligible broadening due to microstrain. This is consistent with the majority of the depth of such films being relaxed, i.e., very low t_{crit}. The RC FWHMs in Fig. 3(c) are also consistent with this, as they reveal little t dependence, the narrow contribution being barely broadened over the STO(001) substrate. Further work will be required to pin down the origin of the broader RC contribution, which is clearly evident (Fig. S2[30]) above $t \approx 100$ Å. This could be related to the expanded a_{op}, potentially reflecting a t-dependent density of defects such as misfit and threading dislocations.

To further probe defects, cross-sectional STEM was performed. Fig. 3(f) shows a representative HAADF STEM image of a 35-Å-thick BSO film, again on STO(001). A smooth, continuous film is evident even at this thickness (~8 unit cells), the major feature of interest being the quite evenly spaced dislocations, marked by arrows. A magnified view of one such dislocation is shown, from which it can be seen that these are misfit edge dislocations with Burger's vector along [100]. The spacing of these dislocations, averaged over multiple images, is 70-80 Å, close to the spacing expected (75 Å) if such misfit dislocations relax the full 5.1% lattice mismatch. This is again consistent with the diffraction observations of very low t_{crit}. STEM imaging of MgO(001)/BSO (supplementary material[30] Fig. S4(a)) reveals a similar picture but with larger dislocation spacing due to the smaller mismatch. As a final comment, it is noted that the low surface roughness from
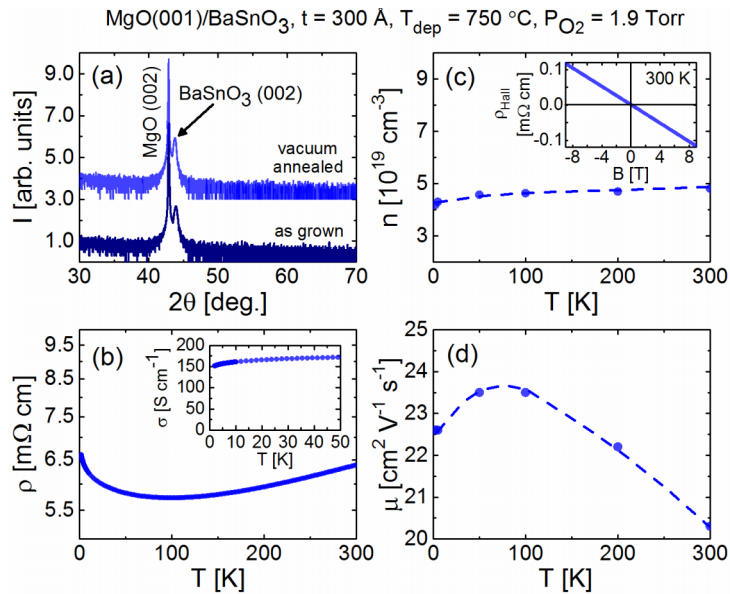
FIG. 4. (a) High resolution WAXRD from a 300-Å-thick MgO(001)/BSO film before and after vacuum annealing at 850 °C. Temperature dependence of (b) the (log scale) film resistivity ρ (c) the Hall electron density n, and (d) the Hall electron mobility μ. Dashed lines are guides to the eye. The insets to (b) show the conductivity, σ, *vs.* temperature below 50 K, and the zero-field-offset-subtracted 300 K Hall resistivity *vs.* magnetic flux density (B), respectively. The growth conditions (750 °C, 1.9 Torr) are labeled at the top. Note that this film was sputtered at 66 W.

STEM (Fig. 3(f)) and GIXR (Fig. 1(c)) is also corroborated by AFM. As shown in Fig. 3(e), a similar 35-Å-thick BSO film on STO(001) has a RMS roughness of only 1.3 Å.

Having established the microstructure of these BSO layers, vacuum annealing was pursued to attempt reduction and *n*-doping. Note that as-deposited films displayed no measurable conduction at any P_{O2} or cooling atmosphere. Vacuum annealing was done for 4 hrs at temperatures from 600 to 900 °C, using MgO(001)/BSO(t = 300 Å) films; no such experiments were performed on STO, due to anticipated complications with V_O formation in the substrates. Consistent with earlier work,[9] no measurable conduction was induced below 600 °C. Above this, finite resistivity was detected, decreasing rapidly with annealing temperature. We focus here, as an illustrative example, on 850 °C reduction. As shown in Fig. 4(a), the WAXRD data are largely unchanged after this vacuum annealing, confirming, within the limits of WAXRD, that no secondary phases form. This is strengthened by analytical STEM using energy dispersive X-ray analysis (supplementary material[30] Figs. S4(b)-S4(e)), which also detects no chemical inhomogeneity after annealing. The lattice parameter does change though, increasing by 0.009 Å, consistent with V_O formation.

Electronic transport reveals large changes in resistivity (ρ) and electron density (n) after annealing, implying reduction to BaSnO$_{3-\delta}$ and facile *n*-doping. As shown in Fig. 4(b), room temperature ρ values are ~6 mΩ cm after 850 °C annealing, in comparison to unmeasurably high values (>15 kΩ cm) as-deposited. ρ decreases on cooling to ~100 K, below which it undergoes a weak upturn, to 6.5 mΩ cm at 2 K. The weak temperature (T) dependence suggests degenerate doping and in fact, the $T \rightarrow 0$ extrapolation of the conductivity, σ, is finite (inset to Fig. 4(b)), implying metallic behavior. Hall effect measurements further elucidate this. A clear, field-linear Hall signal due to electrons is observed (inset to Fig. 4(c)), n varying only weakly with T (Fig. 4(c)), consistent with degenerate doping. Additionally, although uncertainty in the effective mass and dielectric constant results in uncertainty in the Mott prediction for the critical electron density in BSO, our upper bound is ~10^{18} cm^{-3}. The observed n (5×10^{19} cm^{-3}, Fig. 4(c)) exceeds this, consistent with the metallicity deduced from the inset to Fig. 4(b). Both this observation and the field-linearity of the Hall voltage are consistent with relatively modest compensation. As shown in Fig. 4(d), the deduced mobility (μ) is around 20.5 cm^2 V^{-1} s^{-1} at 300 K, increasing to 23.5 cm^2 V^{-1} s^{-1} at 50-100 K, before decreasing to 22.5 cm^2 V^{-1} s^{-1} at low T. Indications of phonon scattering contributions to

the mobility are thus found, although scattering from defects such as dislocations is likely also important. In addition to establishing that V_O formation is facile in BSO and that it enables *n*-doping without impurities, these results point to numerous viable approaches to improve mobility. Substrate choice, thickness, and reduction temperature are obvious optimization variables, with the potential to elucidate the range of *n* obtainable by reduction, the resulting μ variation, the quantitative influence of misfit and threading dislocations, and, ultimately, the relative impact of the various defects on mobility.

In summary, we have demonstrated the growth of epitaxial, phase pure, relaxed, close to stoichiometric BSO films on STO(001) and MgO(001) using high pressure oxygen sputter deposition. A detailed picture of the microstructure is provided, particularly with respect to strain relaxation *via* misfit dislocations. Importantly, vacuum annealing at 850 °C is found to induce oxygen vacancies at significant densities, without secondary phase formation, enabling facile *n*-doping. Mobilities of 20 cm^2 V^{-1} s^{-1} at 5×10^{19} cm^{-3} are obtained in films only 300 Å thick, with much scope for improvement. Ultimately, this will enable a comparison of electronic properties obtainable by intrinsic *vs.* extrinsic doping in BSO, an important step for room temperature applications.

[1] T. Makino, Y. Segawa, A. Tsukazaki, A. Ohtomo, and M. Kawasaki, Appl. Phys. Lett. **87**, 022101 (2005).
[2] A. Tsukazaki, A. Ohtomo, T. Kita, Y. Ohno, H. Ohno, and M. Kawasaki, Science **315**, 1388 (2007).
[3] J. Falson, D. Maryenko, Y. Kozuka, A. Tsukazaki, and M. Kawasaki, Appl. Phys. Express **4**, 091101 (2011).
[4] A. Tsukazaki, S. Akasaka, K. Nakahara, Y. Ohno, H. Ohno, D. Maryenko, A. Ohtomo, and M. Kawasaki, Nat. Mater. **9**, 889 (2010).
[5] P. D. C. King and T. D. Veal, J. Phys.: Condens. Matter **23**, 334214 (2011).
[6] J. A. Sulpizio, S. Ilani, P. Irvin, and J. Levy, Annu. Rev. Mater. Res. **44**, 117 (2014).
[7] R. Ramesh and D. G. Schlom, MRS Bull. **33**, 1006 (2008).
[8] H. Y. Hwang, Y. Iwasa, M. Kawasaki, B. Keimer, H. Nagaosa, and Y. Tokura, Nat. Mater. **11**, 103 (2012).
[9] H. J. Kim, U. Kim, H. M. Kim, T. H. Kim, H. S. Mun, B. G. Jeon, K. T. Hong, W. J. Lee, C. Ju, K. H. Kim, and K. Char, Appl. Phys. Express **5**, 061102 (2012).
[10] H. J. Kim, U. Kim, T. H. Kim, J. Kim, H. M. Kim, B.-G. Jeon, W.-J. Lee, H. S. Mun, K. T. Hong, J. Yu, K. Char, and K. H. Kim, Phys. Rev. B **86**, 165205 (2012).
[11] X. Luo, Y. S. Oh, A. Sirenko, P. Gao, T. A. Tyson, K. Char, and S.-W. Cheong, Appl. Phys. Lett. **100**, 172112 (2012).
[12] A. Spinelli, M. A. Torija, C. Liu, C. Jan, and C. Leighton, Phys. Rev. B **81**, 155110 (2010).
[13] U. Kim, C. Park, T. Ha, R. Kim, H. S. Mun, H. M. Kim, H. J. Kim, T. H. Kim, N. Kim, J. Yu, K. H. Kim, J. H. Kim, and K. Char, APL Mater. **2**, 056107 (2014).
[14] H. Mun, U. Kim, H. M. Kim, C. Park, T. H. Kim, H. J. Kim, K. H. Kim, and K. Char, Appl. Phys. Lett. **102**, 252105 (2013).
[15] P. V. Wadekar, J. Alaria, M. O'Sullivan, N. L. O. Flack, T. D. Manning, L. J. Phillips, K. Durose, O. Lozano, S. Lucas, J. B. Claridge, and M. J. Rosseinsky, Appl. Phys. Lett. **105**, 052104 (2014).
[16] R. J. Cava, P. Gammel, B. Batlogg, J. J. Krajewski, W. F. Peck, L. W. Rupp, R. Felder, and R. B. van Dover, Phys. Rev. B **42**, 4815 (1990).
[17] T. N. Stanislavchuk, A. A. Sirenko, A. P. Litvinchuk, X. Luo, and S.-W. Cheong, J. Appl. Phys. **112**, 044108 (2012).
[18] E. Moreira, J. M. Henriques, D. L. Azevedo, E. W. S. Caetano, V. N. Freire, and E. L. Albuquerque, J. Solid State Chem. **187**, 186 (2012).
[19] H. R. Liu, J. H. Yang, H. J. Xiang, X. G. Gong, and S. H. Wei, Appl. Phys. Lett. **102**, 112109 (2013).
[20] H. Mizoguchi, P. Chen, P. Boolchand, V. Ksenofontov, C. Felser, P. W. Barnes, and P. M. Woodward, Chem. Mater. **25**, 3858 (2013).
[21] D. J. Singh, Q. Xu, and K. P. Ong, Appl. Phys. Lett. **104**, 011910 (2014).
[22] Y. Li, L. Zhang, Y. Ma, and D. J. Singh, APL Mater. **3**, 011102 (2015).
[23] L. Bjaalie, B. Himmetoglu, L. Weston, A. Janotti, and C. G. VandeWalle, New J. Phys. **16**, 025005 (2014).
[24] X. Fan, W. Zheng, X. Chen, and D. J. Singh, PLoS One **9**, e91423 (2014).
[25] S. Sallis, D. O. Scanlon, S. C. Chae, N. F. Quackenbush, D. A. Fischer, J. C. Woicik, J. H. Guo, S. W. Cheong, and L. F. J. Piper, Appl. Phys. Lett. **103**, 042105 (2013).
[26] H. F. Wang, Q. Z. Liu, F. Chen, G. Y. Gao, W. Wu, and X. H. Chen, J. Appl. Phys. **101**, 106105 (2007).
[27] H. J. Kim, J. Kim, T. H. Kim, W. J. Lee, B. G. Jeon, J. Y. Park, W. S. Choi, D. W. Jeong, S. H. Lee, J. Yu, T. W. Noh, and K. H. Kim, Phys. Rev. B **88**, 125204 (2013).
[28] D. O. Scanlon, Phys. Rev. B **87**, 161201 (2013).
[29] M. Bjorck and G. Andersson, J. Appl. Crystallogr. **40**, 1174 (2007).
[30] See supplementary material at http://dx.doi.org/10.1063/1.4919969 for details of structural characterizations of films on both SrTiO$_3$ and MgO substrates.